Constraints on active-sterile neutrino transition magnetic moments from low-energy electronic recoils at direct detection experiments

M. F. Mustamin [a] **and M. Demirci**, [b,1]

[a]Graduate School of Natural and Applied Science, Karadeniz Technical University, Trabzon 61080, Türkiye

[b]Department of Physics, Karadeniz Technical University, Trabzon 61080, Türkiye

E-mail: mfmustamin@ktu.edu.tr, mehmetdemirci@ktu.edu.tr

Abstract. Sterile neutrinos can potentially be produced through neutrino transition magnetic moments in neutrino–electron scattering. In this work, we probe such interactions for sterile neutrinos in the low-mass regime using low-energy electronic recoil data from direct detection experiments. We derive robust constraints on the active-sterile neutrino transition magnetic moments, scrutinizing PandaX-4T and XENONnT recent datasets. Detailed statistical analyses are performed, providing exclusion limits at both one and two degrees of freedom. We demonstrate that, as we can distinguish neutrino flavors, direct detection experiments offer a unique framework for studying all possible neutrino flavors. The obtained limits are in agreement with existing results in the literature and extend the sensitivity to previously unexplored regions of the parameter space.

Keywords: sterile dipole portal, dark matter experiments, solar and atmospheric neutrinos

[1]Corresponding author.

Contents

1 Introduction

Direct detection (DD) experiments, which are intended to search for dark matter (DM), are undergoing rapid development. These detectors are typically located deep underground to mitigate background from cosmic rays and cosmogenic radiation. Their primary goal is to measure electronic or nuclear recoil signals resulting from potential interactions between dark matter particles and detector target materials. Moreover, as neutrinos constitute an irreducible background in these experiments, DD facilities offer a valuable platform to probe neutrino properties. In particular, they enable the study of solar neutrino interactions, allowing precision measurements of the Standard Model (SM) weak mixing angle at the lowest accessible energies, and provide sensitivity to potential contributions from new neutrino interactions beyond the SM (BSM).

The discovery of neutrino oscillations [1–3] provides compelling evidence that neutrinos possess nonzero masses. This observation stands in clear contrast to the prediction of the SM, in which neutrinos are massless because only left-handed neutrinos participate in weak interactions. Explaining this phenomenon therefore requires an extension of the SM. In many BSM frameworks, the mechanisms that generate neutrino masses invoke the existence of additional heavy neutral leptons, commonly referred to as sterile neutrinos [4–6]. The sterile neutrino hypothesis is further motivated by its potential to resolve several anomalies observed in short-baseline oscillation and reactor facilities, including MiniBooNE [7], MicroBooNE [8], and LSND [9]. The proposed particle, capable of explaining these anomalies, would typically possess mass in the eV scale, with a possible connection to nucleosynthesis processes in core-collapse supernovae [10, 11]. Furthermore, sterile neutrinos in the higher mass regime have been proposed as viable dark matter candidates [12]. Beyond these contexts, the sterile neutrino framework has been extensively studied in various theoretical scenarios, including its role in inducing effective neutrino magnetic moments [13], connections to extra dimensions [14], and its influence on the early universe's thermal history and evolution [15].

One possible process for producing sterile neutrinos is through the up-scattering [16, 17] of active neutrinos off electrons via transition magnetic moments [18]. This process is conceptually related to the Primakoff up-scattering mechanism, originally proposed for studying photoproduction of neutral mesons in a nuclear electric field [19]. Investigating this phenomenon via electronic recoil signals in DD experiments is of particular interest, as it offers a novel avenue to constrain active-sterile neutrino transition magnetic moments and related parameters. This transition magnetic moment has been broadly studied using data from a wide range of experiments. Some of them include accelerator-based neutrino sources [20–22], neutral-current ν_μ–nucleus scattering experiments [23], spallation neutron sources [24], nuclear reactors [25–27], forward neutrino detection facilities [28], high-energy particle colliders [29], and atmospheric neutrino observations [30–33]. Additionally, several studies investigated this scenario using previous DD results [34, 35], as well as utilizing cosmological neutrino sources [36], neutrino telescope observations [37], and the diffuse supernova neutrino background [38].

Prompted by the aforementioned motivations, we probe the contribution of active-sterile neutrino transition magnetic moments to the elastic neutrino–electron scattering (EνES) framework, utilizing recent low-energy electronic recoil signals from DD experiments. As one of the irreducible backgrounds in DD experiments, EνES events induced by solar neutrinos provide a natural framework to probe active-sterile neutrino transition magnetic moments. Particularly, we focus on the PandaX-4T [39] and XENONnT [40] recent datasets, deriving new limits on the transition magnetic moment and further tightening available results in the literature. We have applied these datasets in our previous studies [41, 42] to explore other new physics scenarios. Moreover, given that solar neutrino oscillations allow the incoming flux to exhibit a flavor composition at Earth, we perform both flavor-independent and flavor-dependent analyses. Furthermore, we discuss the derived limits with the existing constraints obtained from various facilities. These include data from CHARM-II [43], NOMAD [44], BOREXINO [45], TEXONO [46], IceCube [47], Dresden-II [48], and CONUS+ [49]. We also provide limits from sterile neutrino decay searches using solar [50] and atmospheric [51] neutrinos, and recent CEνNS-induced solar neutrino measurements at PandaX-4T [52] and XENONnT [53], as well as other astrophysical and cosmological bounds.

The outline of this work is the following. We briefly explain in Sec. 2 the EνES process in the SM and in the up-scattering process through the active-sterile neutrino transition magnetic moment. We then provide the details for data analysis in Sec. 3. In Sec. 4, we discuss the predicted event rates and our derived limits of the parameters. We conclude our work in Sec. 5.

2 Theoretical Framework

2.1 EνES in the SM

The process of EνES has a nature of being extremely directional. The scattered electrons have very small angles relative to the incoming neutrinos' direction [54]. This property has been utilized in many neutrino experiments, particularly for solar neutrino detections at Super-Kamiokande [55, 56], SNO [57, 58], and BOREXINO [45, 59]. Furthermore, the coming solar neutrinos can induce EνES events in DD experiments of DM as they collide with the target material in a detector. This process, together with coherent neutrino-nucleus scattering, is one of the neutrino background components in the DD experiments. Therefore, signals of neutrino-electron scatterings have a degeneracy with the DM-electron scatterings.

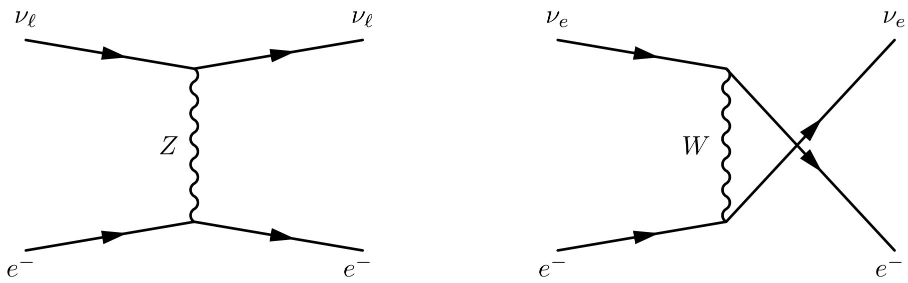

(a) (b)

Figure 1. Representative diagrams for EνES in the SM via (a) NC and (b) CC channels.

The EνES processes are purely leptonic interactions within the SM. We present the tree-level Feynman diagrams of the scatterings in Fig. 1. The index ℓ runs for e, μ, or τ flavor of neutrino. The coming neutrinos ν_ℓ scatter off electrons e^- through charged-current (CC) or neutral-current (NC) channels, depending on the neutrino flavor. The neutral gauge boson is represented by Z, while the charged gauge boson is W. The differential cross-section of the SM process is given by

$$\left[\frac{d\sigma_{\nu_\ell}}{dT_e}\right]_{\rm SM} = \frac{G_F^2 m_e}{2\pi}\left[(g_V + g_A)^2 + (g_V - g_A)^2\left(1 - \frac{T_e}{E_\nu}\right)^2 - (g_V^2 - g_A^2)\frac{m_e T_e}{E_\nu^2}\right], \tag{2.1}$$

where T_e is the electron recoil energy, m_e is the electron mass, E_ν is the energy of the incoming neutrino, and G_F is the Fermi coupling constant [60]. The vector and axial-vector couplings to specific neutrino flavors are

$$g_V = -\frac{1}{2} + 2s_W^2 + \delta_{\ell e} \quad \text{and} \quad g_A = -\frac{1}{2} + \delta_{\ell e}, \tag{2.2}$$

respectively. We adopt the abbreviation $s_W = \sin\theta_W$, where θ_W denotes the weak mixing angle. These couplings depend on the incoming neutrino's flavor. The Kronecker delta symbol $\delta_{\ell e}$ stands for the NC ($\ell = e$) and CC ($\ell = \mu, \tau$) nature of the process. Taking radiative corrections into account, we use flavor-dependent couplings $g_V^{\nu_e e} = 0.9524, g_A^{\nu_e e} = 0.4938, g_V^{\nu_\mu e} = -0.0394, g_A^{\nu_\mu e} = -0.5062, g_V^{\nu_\tau e} = -0.0350$, and $g_A^{\nu_\tau e} = -0.5062$ [61–63]. We emphasize that for ν_e both NC and CC contribute to the calculation, while for the ν_μ and ν_τ only the NC contributes.

2.2 Sterile neutrino dipole portal

The active-sterile neutrino transition magnetic moments could be investigated by electromagnetically up-scattered neutrino beams on electrons. The effective operator at low-energy of such interactions can be written as [27]

$$\mathcal{L}_{\rm int} \supset \frac{\mu_{\nu_{\ell 4}}}{2}\bar{\nu}_{\ell L}\sigma^{\mu\nu}P_R\nu_4 F_{\mu\nu} + \text{h.c.}. \tag{2.3}$$

The coupling of the transition magnetic moment is represented by $\mu_{\nu_{\ell 4}}$, while ν_4 denotes the sterile neutrino, $\nu_{\ell L}$ the SM neutrino, and $F_{\mu\nu}$ the electromagnetic field tensor. It should be emphasized that this form is suitable at low energies only, typically less than the electroweak (EW) energy. The EνES process considered here involves an incoming neutrino with low energy, and hence the formulation remains applicable.

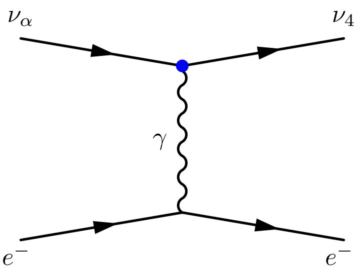

Figure 2. Representative diagram for the up-scattering of $\nu_\ell + e^- \to \nu_4 + e^-$. The dotted vertex represents the neutrino dipole portal of the active-sterile neutrino transition magnetic moment.

We show in Fig. 2 the representative diagram of the up-scattering process of EνES through $\mu_{\nu_{\ell 4}}$. The initial active neutrino ν_ℓ, through a sterile neutrino dipole portal, exchanges a photon with the target electron and up-scatters to the final sterile neutrino ν_4. We can write the process's amplitude as

$$i\mathcal{M} = \mu_{\nu_{\ell 4}} \left(\bar{u}_{\nu_4} \sigma^{\mu\nu} P_L q_\nu u_{\nu_\ell}\right) \left(\frac{-i g_{\mu\lambda}}{q^2}\right) j_e^\lambda, \tag{2.4}$$

with the leptonic current $j_e^\lambda = -ie(\bar{u}_e \gamma^\lambda u_e)$. The differential cross-section of the process is

$$\begin{aligned} \left[\frac{d\sigma(E_\nu, T_e)}{dT_e}\right] = & \frac{\pi\alpha_{\mathrm{EM}}^2}{m_e^2} \left|\frac{\mu_{\nu_{\ell 4}}}{\mu_B}\right|^2 \left[\frac{1}{T_e} - \frac{1}{E_\nu} - \frac{m_4^2}{2T_e E_\nu m_e}\left(1 - \frac{T_e}{2E_\nu} + \frac{m_e}{2E_\nu}\right)\right. \\ & \left. - \frac{m_4^4}{8 m_e T_e^2 E_\nu^2}\left(1 - \frac{T_e}{m_e}\right)\right], \end{aligned} \tag{2.5}$$

where the factor of $\pi\alpha_{\mathrm{EM}}/m_e^2$ arises from normalizing the magnetic moments in terms of the Bohr magneton, μ_B. We note that in the limit $m_4 = 0$, the expression gives us to the standard case involving only active neutrino scattering, as discussed in Ref. [64]. Additionally, there is a kinematic constraint of the sterile neutrino mass

$$m_4^2 \leq 2 m_e T_e \left(E_\nu \sqrt{\frac{2}{m_e T_e}} - 1\right). \tag{2.6}$$

The contribution from an active-sterile neutrino transition magnetic moment is added coherently to the EμES in the SM, leading to potential enhancements in the predicted event at low-energy electronic recoil signals.

3 Data Analysis Details

3.1 Event Rate

We express the differential event rate per unit target mass as

$$\left[\frac{dR}{dT_e}\right]^i = Z_{\mathrm{eff}}(T_e) \int_{E_\nu^{\mathrm{min}}}^{E_{\nu,i}^{\mathrm{max}}} dE_\nu \frac{d\Phi^i}{dE_\nu} \left[\frac{d\sigma}{dT_e}\right], \tag{3.1}$$

where $d\Phi^i/dE_\nu$ is the differential neutrino flux for the i^{th} solar neutrino component, and $Z_{\mathrm{eff}}(T_e)$ denotes the effective atomic number accounting for the number of available electrons per recoil energy bin in the detector. The differential cross section $d\sigma/dT_e$ includes contributions from both the SM interactions and the additional sterile neutrino dipole portal. In this work, we adopt the free electron approximation for $Z_{\rm eff}(T_e)$, where all atomic electrons are considered unbound and uniformly available for scattering at all recoil energies. This is a valid assumption for electron recoil energies well above the binding energies of atomic shells [65], typically applicable in the energy region considered in this analysis [66, 67]. Under this assumption, the effective atomic number is expressed as

$$Z_{\rm eff}(T_e) = \sum_{\alpha} n_\alpha \theta(T_e - B_\alpha) \tag{3.2}$$

where $\theta(x)$ denotes the step function, n_α the number of electrons in atomic shell α, and B_α the corresponding binding energy. The binding energies and electron occupation numbers for the xenon target material are taken from Ref. [68]. The required minimum neutrino energy to produce a recoil energy with an outgoing sterile neutrino is

$$E_\nu^{\rm min} = \frac{T_e}{2}\left(1 + \sqrt{1 + \frac{2m_e}{T_e}}\right)\left(1 + \frac{m_4^2}{2m_e T_e}\right), \tag{3.3}$$

while the maximum energy $E_{\nu,i}^{\rm max}$ is taken from the neutrino flux endpoint.

The dependence of $E_\nu^{\rm min}$ on T_e is illustrated in Fig. 3. Several masses of the sterile neutrino are chosen to demonstrate the kinematic behavior. As expected, the minimum energy required to produce a recoil is linearly dependent on the increasing electronic recoil. At sufficiently high electron recoil energies, the kinematic threshold approaches the limit corresponding to the massless, active-only, neutrino case (solid-black line). In the recoil energy

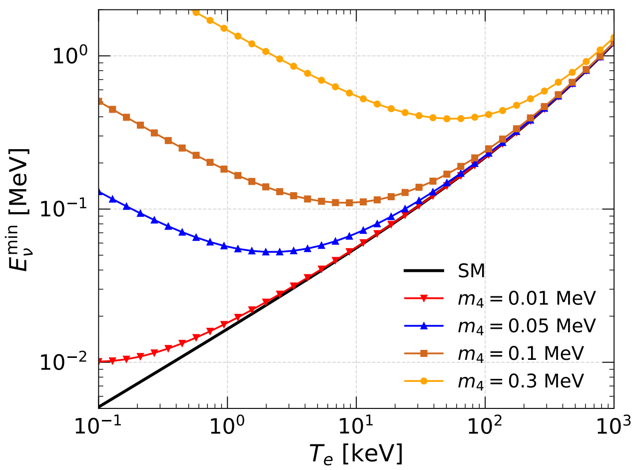

Figure 3. Behavior of the minimum neutrino energy with the electron recoil energy for different values of sterile neutrino masses.

region considered in this work, where $T_e \lesssim 30$ keV, different masses of the sterile neutrino noticeably modify the minimum required neutrino energy, thereby affecting the expected event rates. This dependency becomes particularly relevant in shaping the observable recoil spectrum, as heavier sterile neutrinos progressively suppress low-energy events due to the increasingly restrictive kinematic threshold.

During their propagation from the Sun to the Earth, neutrinos experience flavor oscillations. Consequently, solar neutrinos arrive as a mixture of all possible flavors at the detector.

The differential cross section needs to be multiplied by the corresponding oscillation probabilities

$$\left[\frac{d\sigma}{dT_e}\right]_X^{\nu e} = P_{ee}\left[\frac{d\sigma_{\nu_e}}{dT_e}\right]_X + \sum_{f=\mu,\tau} P_{ef}\left[\frac{d\sigma_{\nu_f}}{dT_e}\right]_X . \tag{3.4}$$

The P_{ee} denotes the survival probability for ν_e, and P_{ef} for an initial ν_e converting into a ν_f flavor ($f = \mu, \tau$) at detection. These transition probabilities are given by $P_{e\mu} = (1-P_{ee})\cos^2\vartheta_{23}$ and $P_{e\tau} = (1-P_{ee})\sin^2\vartheta_{23}$, respectively. The electron neutrino survival probability, accounting for both vacuum and matter effects, is expressed as [69]

$$\begin{aligned} P_{ee} =& \cos^2(\vartheta_{13})\cos^2(\vartheta_{13}^m)\left(\frac{1}{2}+\frac{1}{2}\cos(2\vartheta_{12}^m)\cos(2\vartheta_{12})\right) \\ &+ \sin^2(\vartheta_{13})\sin^2(\vartheta_{13}^m), \end{aligned} \tag{3.5}$$

where the neutrino mixing angles are given by $\vartheta_{12}, \vartheta_{13}$ and ϑ_{23}, while the superscript m indicates quantities evaluated in the solar matter environment. In our calculation, we account for the day–night asymmetry, coming from the regeneration of ν_e through coherent forward scattering with Earth's matter during nighttime propagation. We use the normal mass ordering scenario for the neutrino oscillation parameters, which are taken from the global 3-flavor fit provided by NuFit-5.3 [70], excluding the Super-Kamiokande atmospheric neutrino dataset for consistency with direct detection analyses.

The predicted number of events in the k^{th} electron recoil energy bin is calculated as

$$R_X^k = \varepsilon N_t \int_{T_e^k}^{T_e^{k+1}} dT_e\ \mathcal{A}(T_e) \int_0^{T_e^{\prime\max}} dT_e'\ \mathcal{R}(T_e, T_e') \sum_{i=pp,{}^7\mathrm{Be}} \left[\frac{dR}{dT_e'}\right]_X^i , \tag{3.6}$$

where N_t is the number of target electrons per unit detector mass. The variables T_e and T_e' denote the reconstructed and true electron recoil energies, respectively. The functions $\mathcal{A}(T_e)$ account for the detector acceptance (efficiency), while $\mathcal{R}(T_e, T_e')$ is the energy resolution (smearing) function The detector efficiency for PandaX-4T is taken from Ref. [39] and XENONnT from Ref. [40]. We consider a normalized Gaussian smearing function for the energy resolution with energy-dependent widths given by $\sigma = 0.073 + 0.173T_e - 0.0065T_e^2 + 0.00011T_e^3$ (in keV) for PandaX-4T [71] and $\sigma = 0.31\sqrt{T_e} + 0.0037T_e$ [72] for XENONnT. In order to compute the total event yield reported by each experiment, we need to multiply the differential event rate by the exposure factor ε. The PandaX-4T Run0 and Run1 datasets correspond to exposures of 198.9 ton $\cdot$ day and 363.3 ton $\cdot$ day, respectively, while the XENONnT SR0 dataset has an exposure of 1.16 ton$\cdot$ year. The maximum allowed recoil energy is determined by kinematics and satisfies

$$T_e^{\prime\max} = \frac{2E_\nu^2}{2E_\nu + m_e}. \tag{3.7}$$

This relation highlights that for a given neutrino energy, lighter targets yield higher maximum recoil energies, although in this context the target electrons are identical for both detectors.

3.2 χ^2 Function

To derive constraints on the new physics parameter(s) of interest, denoted by $\mathcal{S}$, we employ a Poisson-based χ^2 test statistic [73, 74], which is defined as

$$\begin{aligned}\chi^2(\mathcal{S}) = \min_{(\alpha_i,\beta_j)} 2\sum_{k=1}^{30}\left[R^k_{\exp}(\mathcal{S};\alpha,\beta) - R^k_{obs} + R^k_{obs}\ln\left(\frac{R^k_{obs}}{R^k_{\exp}(\mathcal{S};\alpha,\beta)}\right)\right] \\ + \sum_i\left(\frac{\alpha_i}{\sigma_{\alpha_i}}\right)^2 + \sum_j\left(\frac{\beta_j}{\sigma_{\beta_j}}\right)^2,\end{aligned} \tag{3.8}$$

where $R^k_{\rm obs}$ and $R^k_{\rm exp}$ represent the observed and expected event rates in the k^{th} energy bin, respectively. The expected rate consists of SM prediction $R^k_{\rm SM}$, the contribution from the transition magnetic moment (TMM) denoted by $R^k_{\rm TMM}$, and other background components $R_{\rm Bkg}$. Explicitly, it is given by $R^k_{\rm exp}(\mathcal{S};\alpha_i,\beta_j) = (1+\alpha_i)(R^k_{\rm SM} + R^k_{\rm BSM}(\mathcal{S})) + (1+\beta_j)R^k_{{\rm Bkg},j}$ in which α_i and β_j are nuisance parameters corresponding to the uncertainties on the solar neutrino fluxes and the individual background components, respectively. The observed data points are taken from Fig.2 of Ref.[39] for PandaX-4T, and from Fig. 4 (and Fig.5) of Ref.[40] for XENONnT, considering recoil energies up to 30 keV. The uncertainty σ_α corresponds to the fractional uncertainties in the solar neutrino fluxes, as listed in Table 6 of Ref. [75], while σ_β represents the associated experimental background uncertainties. The total predicted event rates—including both the SM and new physics contributions—are calculated using solar neutrino fluxes from Bahcall's spectrum [76], normalized according to the B16-GS98 Standard Solar Model [75].

4 Results

In this section, we present our numerical results for the active–sterile neutrino transition magnetic moment based on the analysis of data from direct detection experiments. We first examine the expected event spectra induced by neutrino-electron scattering. We then discuss our derived limits from analyzing recent electronic recoil signals from PandaX-4T (Run0 and Run1) and XENONnT.

4.1 Expected event spectra

In Fig. 4, we show the electron recoil data from PandaX-4T and XENONnT together with the expected event rates in the presence of the active–sterile neutrino transition magnetic moment. The predicted EνES signals induced by solar neutrinos are subtracted from the total background reported by each experiment. They are shown as dashed black lines, exhibiting good agreement with the results published by the respective collaborations. In investigating the sensitivity to possible active–sterile neutrino transition magnetic moments, we have considered several benchmarks with sterile neutrino mass of 0.1 MeV and transition magnetic moments of $3\times10^{-11}\mu_B$.

We consider both flavor-dependent and flavor-independent cases. In the flavor-dependent case, limits are individually derived for each active neutrino flavor, treating $\mu_{\nu_{e4}}$, $\mu_{\nu_{\mu4}}$, and $\mu_{\nu_{\tau4}}$ as independent parameters, with marginalization performed over the remaining flavor components. In the flavor-independent (universal coupling) case, $\mu_{\nu_{\ell4}} = \mu_{\nu_{e4}} = \mu_{\nu_{\mu4}} = \mu_{\nu_{\tau4}}$. This scenario yields a single combined spectrum, incorporating contributions from all neutrino flavors weighted by their survival and transition probabilities. The predicted spectra for each

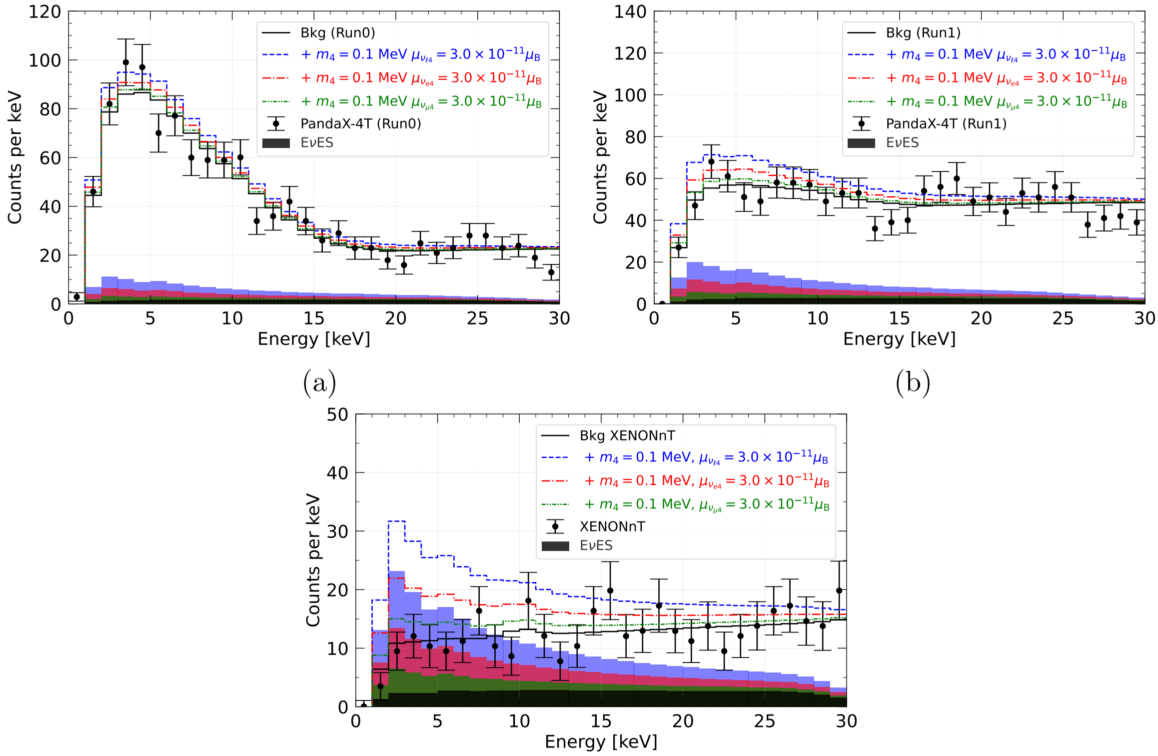

Figure 4. Predicted electron recoil spectra from EνES in the presence of active–sterile transition magnetic moments, compared to the measured data from (a) PandaX-4T Run0, (b) PandaX-4T Run1, and (c) XENONnT. Individual contributions to the EνES are shown as filled colored histograms, while their corresponding contributions to the total background are represented by empty, outlined histograms in the same colors.

flavor-specific transition magnetic moment are shown as colored lines in the figure to distinguish their contributions. As expected, the enhancement in event rates due to the presence of a transition magnetic moment is most prominent at low recoil energies. This highlights the importance of improving experimental sensitivity in this region for future searches. The current datasets already provide useful constraints on probing scenarios involving neutrino electromagnetic interactions beyond the SM.

4.2 Constraints on the sterile neutrino dipole portal

We now discuss the limits we have derived on the active–sterile neutrino transition magnetic moments. As mentioned earlier, both flavor-dependent and flavor-independent scenarios are considered. This classification is motivated by the properties of solar neutrinos, which contribute to the background components observed in direct detection experiments. In our analysis, we employ the most recent low-energy electron recoil datasets from the PandaX-4T (Run0 and Run1) and XENONnT experiments. These experiments offer unprecedented sensitivity to neutrino–electron scattering processes at recoil energies below 30 keV.

We also compare our derived limits with existing constraints reported in the literature. Previous studies have employed data from a variety of experimental platforms, including the COHERENT experiment at the Spallation Neutron Source (CsI and LAr detectors) [24]; reactor-based experiments utilizing both EνES and CEνNS processes, such as CONUS+ [25]

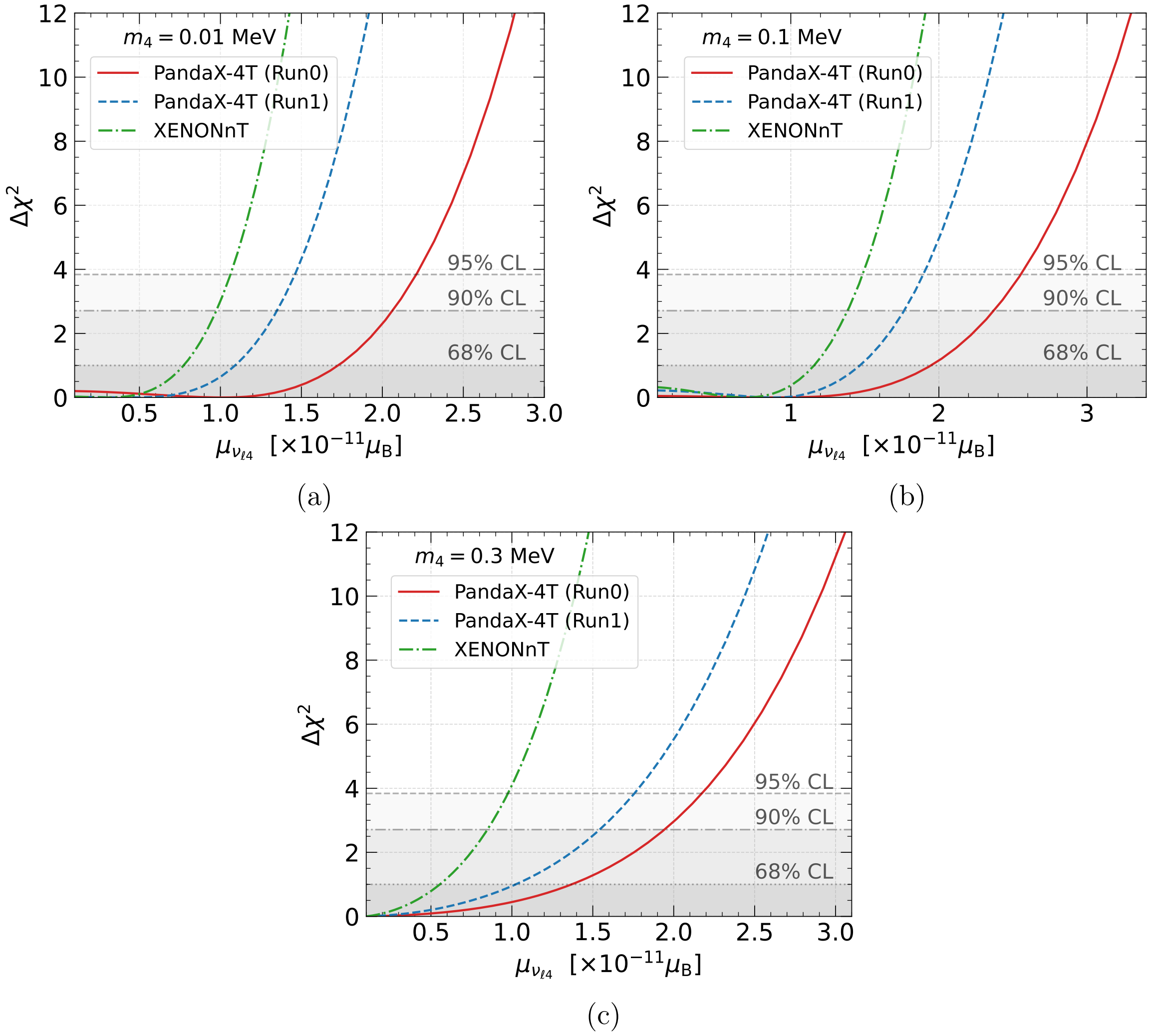

Figure 5. The likelihood profile of the effective active-transition magnetic moment $\mu_{\nu_{\ell 4}}$, obtained from PandaX-4T Run0, PandaX-4T Run1, and XENONnT data, for (a) $m_4 = 0.01$ MeV, (b) $m_4 = 0.1$ MeV, and (c) $m_4 = 0.3$ MeV.

and Dresden-II (FeF) [26], as well as those relying solely on EνES, such as TEXONO [34]; the solar neutrino experiment BOREXINO [36]; and accelerator-based experiments including LSND (95% CL) [20] and CHARM-II [30]. Additional constraints have also been obtained from other facilities such as MiniBooNE [20], NOMAD [17] and IceCube [30]. Furthermore, we include comparisons with indirect limits derived from sterile neutrino decay signatures using solar [31] and atmospheric [32] neutrino data. For completeness, we also mention astrophysical bounds from SN1987A [20] and cosmological observations [36].

By setting a different mass scale for the effective sterile neutrino dipole portal, we present the 1 dof limits of the active-sterile neutrino magnetic moment in Fig. 5. As can be seen from Fig. 5(a), for $m_4 = 0.01$ MeV, we obtain the 90% CL limits as $\mu_{\nu_{\ell 4}} \lesssim 2.06 \times 10^{-11}\mu_B$ for PandaX-4T Run0, $\mu_{\nu_{\ell 4}} \lesssim 1.35 \times 10^{-11}\mu_B$ for PandaX-4T Run1, and $\mu_{\nu_{\ell 4}} \lesssim 0.97 \times 10^{-11}\mu_B$ for XENONnT. In Fig. 5(b), for $m_4 = 0.1$ MeV, we find the 90% CL limits to be $\mu_{\nu_{\ell 4}} \lesssim 2.37 \times 10^{-11}\mu_B$ for PandaX-4T Run0, $1.76 \times 10^{-11}\mu_B$ for PandaX-4T Run1 and $\mu_{\nu_{\ell 4}} \lesssim 1.38 \times 10^{-11}\mu_B$ for XENONnT. Similarly, in Fig. 5(c), for $m_4 = 0.3$ MeV, we determine the 90% CL limits

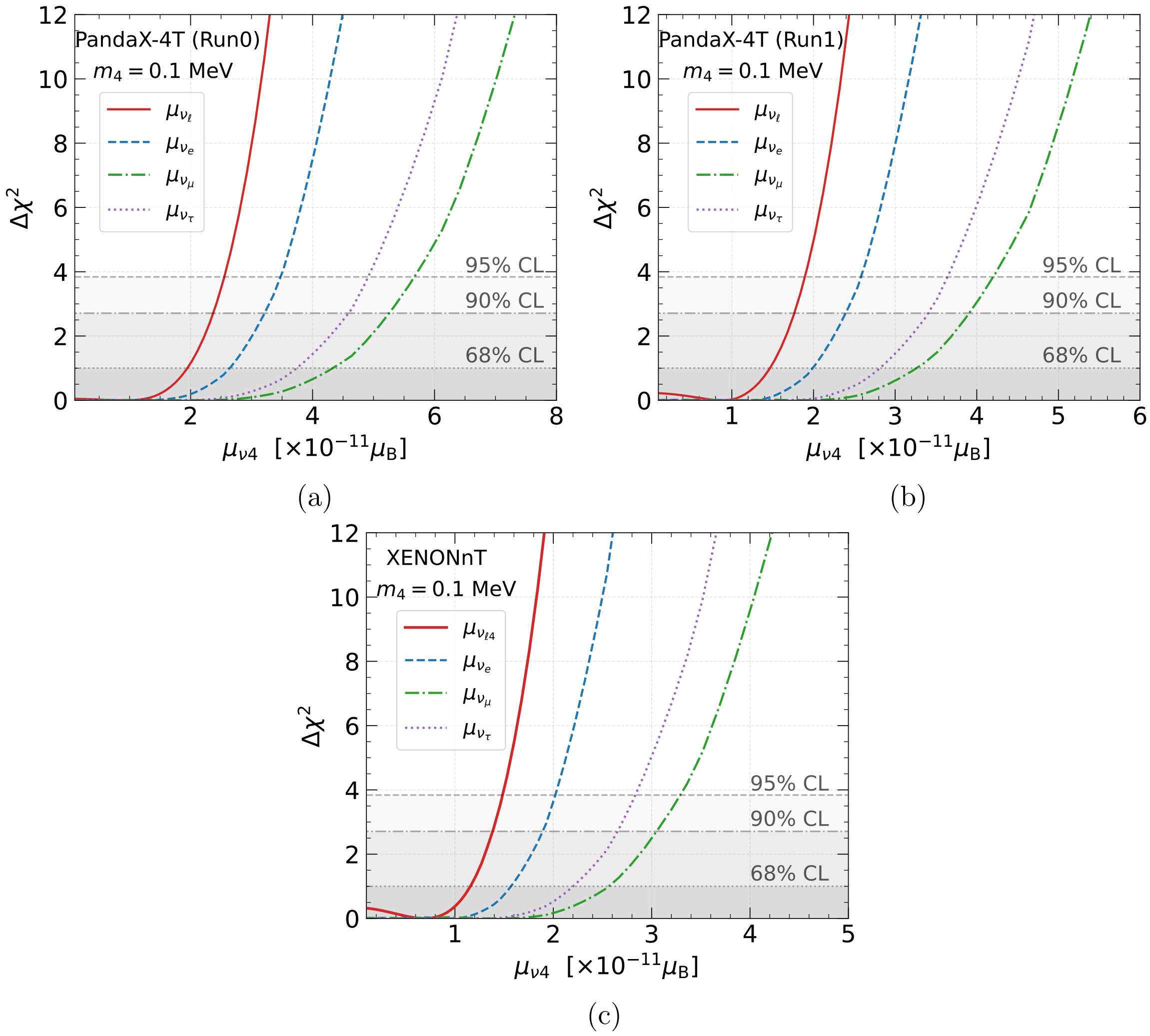

Figure 6. The likelihood profile of the active-transition magnetic moments obtained from (a) PandaX-4T Run0, (b) PandaX-4T Run1, and (c) XENONnT data for $m_4 = 0.1$ MeV.

as $\mu_{\nu_{\ell 4}} \lesssim 1.94 \times 10^{-11}\mu_{\rm B}$ for PandaX-4T Run0, $\mu_{\nu_{\ell 4}} \lesssim 1.54 \times 10^{-11}\mu_{\rm B}$ for PandaX-4T Run1, and $\mu_{\nu_{\ell 4}} \lesssim 0.85 \times 10^{-11}\mu_{\rm B}$ for XENONnT. These results clearly indicate the improvement in sensitivity provided by PandaX-4T Run1 data over Run0, while XENONnT maintains competitive limits across the considered mass values.

Furthermore, we present the 1 dof limits for flavor-dependent cases in Fig. 6, where the mass of the sterile neutrino is fixed at $m_4 = 0.1$ MeV. From PandaX-4T Run0, we obtain the 90% CL limits as $\mu_{\nu_{\ell 4}} \lesssim 2.37 \times 10^{-11}\mu_{\rm B}$, $\mu_{\nu_{e4}} \lesssim 3.21 \times 10^{-11}\mu_{\rm B}$, $\mu_{\nu_{\mu 4}} \lesssim 5.25 \times 10^{-11}\mu_{\rm B}$, and $\mu_{\nu_{\tau 4}} \lesssim 4.59 \times 10^{-11}\mu_{\rm B}$. For PandaX-4T Run1, we find the limits to be $\mu_{\nu_{\ell 4}} \lesssim 1.76 \times 10^{-11}\mu_{\rm B}$, $\mu_{\nu_{e4}} \lesssim 2.39 \times 10^{-11}\mu_{\rm B}$, $\mu_{\nu_{\mu 4}} \lesssim 3.91 \times 10^{-11}\mu_{\rm B}$, and $\mu_{\nu_{\tau 4}} \lesssim 3.40 \times 10^{-11}\mu_{\rm B}$. From XENONnT data, the corresponding limits are $\mu_{\nu_{\ell 4}} \lesssim 1.38 \times 10^{-11}\mu_{\rm B}$, $\mu_{\nu_{e4}} \lesssim 1.89 \times 10^{-11}\mu_{\rm B}$, $\mu_{\nu_{\mu 4}} \lesssim 3.05 \times 10^{-11}\mu_{\rm B}$, and $\mu_{\nu_{\tau 4}} \lesssim 2.65 \times 10^{-11}\mu_{\rm B}$. A summary of these results is provided in Table 1 for clarity and comparison. We clearly observe that, for flavor-dependent case, the sensitivity to $\mu_{\nu_{e4}}$ is consistently stronger than those for $\mu_{\nu_{\mu 4}}$ and $\mu_{\nu_{\tau 4}}$ across all datasets, which is a direct consequence of the dominant contribution of electron-flavor solar neutrinos to electrons in elastic scattering processes. Among the three datasets, PandaX-4T Run1

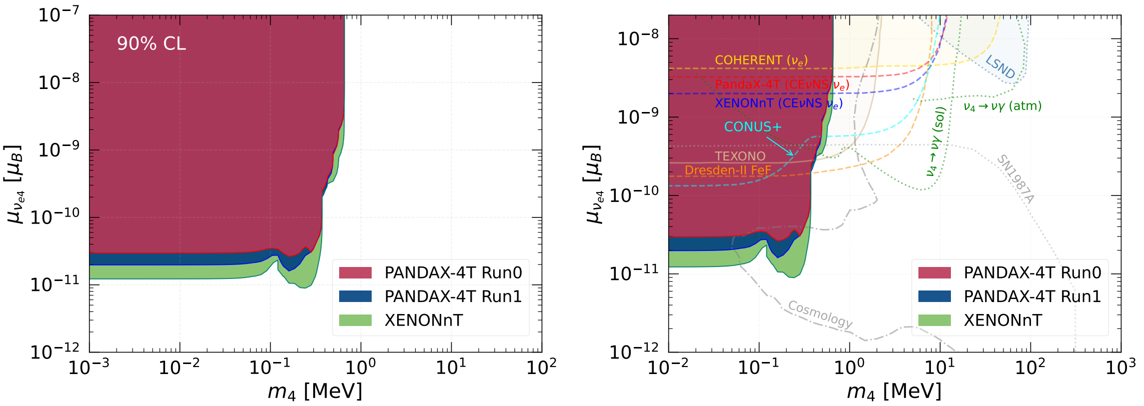

(a) (b)

Figure 7. (a) Exclusion regions with 90% CL (2 dof) on the plane of the $\mu_{\nu_{e4}}$ vs m_4 from PandaX-4T (Run0), (Run1) and XENONnT datasets, and (b) comparison with other available limits (see the text for details).

provides notable improvements over Run0 for all flavor cases, while XENONnT continues to set the most stringent constraints, particularly for $\mu_{\nu_{e4}}$ and $\mu_{\nu_{\ell 4}}$ couplings.

Table 1. Summary of the derived 90% CL limits (1 dof) on the transition magnetic moments for $m_4 = 0.1$ MeV, obtained from the PandaX-4T and XENONnT datasets.

TMM	PandaX-4T		XENONnT
	Run0	Run1	
$\mu_{\nu_{\ell 4}}$	$\lesssim 2.37 \times 10^{-11} \mu_{\rm B}$	$\lesssim 1.76 \times 10^{-11} \mu_{\rm B}$	$\lesssim 1.38 \times 10^{-11} \mu_{\rm B}$
$\mu_{\nu_{e4}}$	$\lesssim 3.21 \times 10^{-11} \mu_{\rm B}$	$\lesssim 2.39 \times 10^{-11} \mu_{\rm B}$	$\lesssim 1.89 \times 10^{-11} \mu_{\rm B}$
$\mu_{\nu_{\mu 4}}$	$\lesssim 5.25 \times 10^{-11} \mu_{\rm B}$	$\lesssim 3.91 \times 10^{-11} \mu_{\rm B}$	$\lesssim 3.05 \times 10^{-11} \mu_{\rm B}$
$\mu_{\nu_{\tau 4}}$	$\lesssim 4.59 \times 10^{-11} \mu_{\rm B}$	$\lesssim 3.40 \times 10^{-11} \mu_{\rm B}$	$\lesssim 2.65 \times 10^{-11} \mu_{\rm B}$

We now discuss the 2 dof results at 90% CL for the electron-flavor case as shown in Fig. 7(a). For $m_4 \lesssim 0.03$ MeV, the derived upper limits are $\mu_{\nu_{e4}} \lesssim 2.97 \times 10^{-11} \mu_{\rm B}$ for PandaX-4T Run0, $\mu_{\nu_{e4}} \lesssim 1.97 \times 10^{-11} \mu_{\rm B}$ for PandaX-4T Run1, and $\mu_{\nu_{e4}} \lesssim 1.22 \times 10^{-11} \mu_{\rm B}$ for XENONnT in the low-mass region. We observe a substantial improvement from PandaX-4T Run0 to Run1, where the upper limit is reduced by more than a factor of two. This enhancement is primarily attributed to the increased exposure and improved background suppression in Run1. Meanwhile, XENONnT delivers the most stringent constraint in this channel, slightly outperforming PandaX-4T Run1, which reflects the advantage of its larger exposure and lower background levels in the relevant low-energy region. In Figure 7(b), we compare our results with previous experimental limits, highlighting the significant improvements achieved by recent datasets—particularly those from PandaX-4T Run 1 and XENONnT. Notably, our derived limits are more stringent than prior constraints in the sub-MeV mass range. Our results are approximately two orders of magnitude more stringent than the limits obtained from CEνNS processes, such as those reported by COHERENT and from solar neutrino–induced backgrounds in PandaX-4T and XENONnT. In comparison to constraints from nuclear reactor experiments—CONUS+, TEXONO, and Dresden-II FeF—the discrepancy is reduced to about one order of magnitude. However, at mass scales $m_4 \gtrsim 1$ MeV, our results do not surpass the existing limits set by LSND and $\nu_4 \to \nu\gamma$ decay searches. Additionally, our constraints partially overlap with the parameter space excluded by SN1987A and cosmological observations.

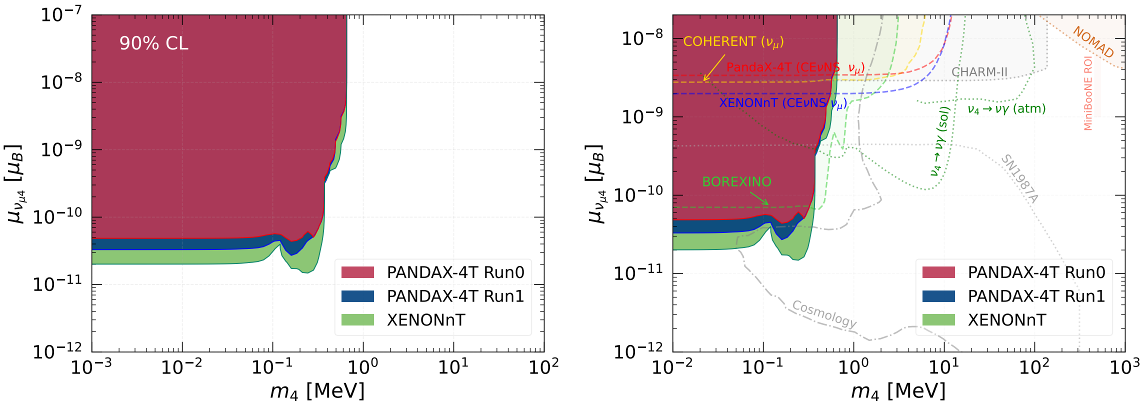

(a) (b)

Figure 8. (a) Exclusion regions with 90% CL (2 dof) on the plane of the $\mu_{\nu_{\mu 4}}$ vs m_4 from PandaX-4T (Run0), (Run1) and XENONnT datasets, and (b) comparison with other available limits (see the text for details).

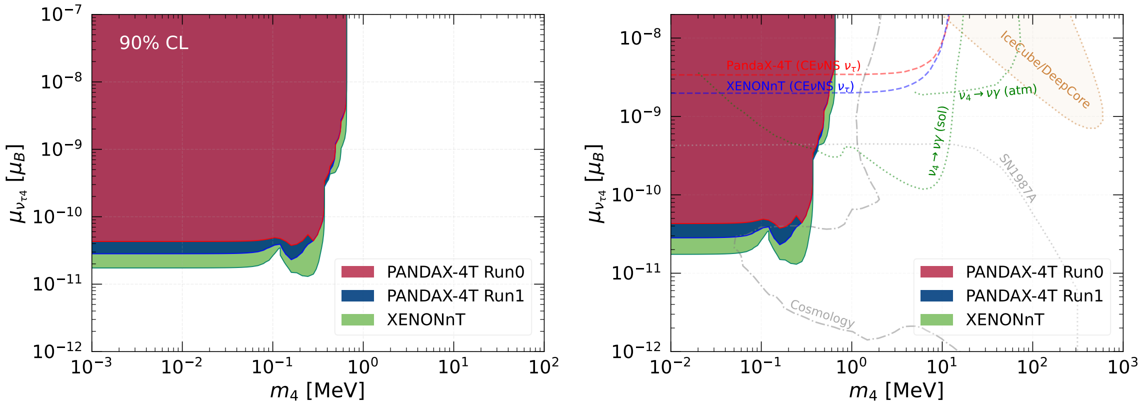

(a) (b)

Figure 9. (a) Exclusion regions with 90% CL (2 dof) on the plane of the $\mu_{\nu_{\tau 4}}$ vs m_4 from PandaX-4T (Run0), (Run1) and XENONnT datasets, and (b) comparison with other available limits (see the text for details).

For the muon-flavor case, we present the 2 dof results at 90% CL in Fig.8(a). The derived upper limits in the region of $m_4 \lesssim 0.03$ MeV are $\mu_{\nu_{\mu 4}} \lesssim 4.86 \times 10^{-11} \mu_B$ for PandaX-4T Run0, $\mu_{\nu_{\mu 4}} \lesssim 3.30 \times 10^{-11} \mu_B$ for PandaX-4T Run1, and $\mu_{\nu_{\mu 4}} \lesssim 2.01 \times 10^{-11} \mu_B$ for XENONnT. We observe a clear improvement in sensitivity from Run0 to Run1, with the upper limit reduced by more than a factor of two. Additionally, XENONnT provides a slightly stronger bound than PandaX-4T Run1, confirming its competitive performance in this channel. A comparison with previous limits is shown in Fig.8(b). Apart from the already mentioned

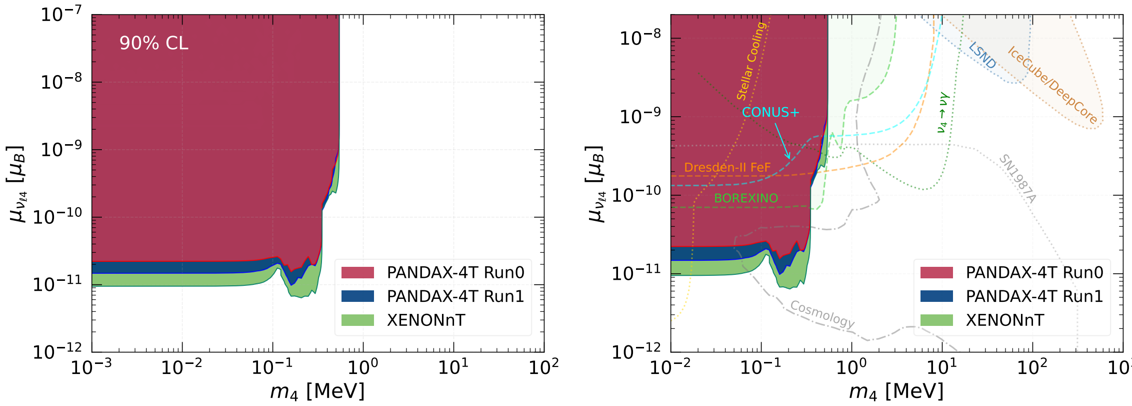

(a) (b)

Figure 10. (a) Exclusion regions with 90% CL (2 dof) on the plane of the $\mu_{\nu_{\ell 4}}$ vs m_4 from PandaX-4T (Run0), (Run1) and XENONnT datasets, and (b) comparison with other available limits (see the text for details).

limits in the electron-flavor case, here we also superimpose additional limits from the solar neutrino experiment and collider facilities. We can see the PandaX-4T Run0 limit is about as sensitive as the BOREXINO limit, while the PandaX-4T Run1 and XENONnT limits provide a few times more stringent results than from this solar neutrino experiment. Meanwhile, limits from CHARM-II, MiniBooNE, and NOMAD dominate at the high-mass region. Regarding the already mentioned limits, we can see similar behavior to the electron-flavor case.

For the tau-flavor case, the 2 dof results at 90% CL are shown in Fig.9(a). The obtained upper limits are $\mu_{\nu_{\tau 4}} \lesssim 4.30 \times 10^{-11}\mu_{\mathrm{B}}$ for PandaX-4T Run0, $\mu_{\nu_{\tau 4}} \lesssim 2.82 \times 10^{-11}\mu_{\mathrm{B}}$ for PandaX-4T Run1, and $\mu_{\nu_{\tau 4}} \lesssim 1.74 \times 10^{-11}\mu_{\mathrm{B}}$ for XENONnT, all in the region of $m_4 \lesssim 0.03$ MeV. Analogous to electron-flavor and muon-flavor cases, we observe a substantial improvement between Run0 and Run1, while XENONnT delivers the most stringent constraint. This result emphasizes the increasing sensitivity of recent direct detection experiments to the tau-flavor sector, which traditionally suffers from weaker constraints due to the absence of direct tau neutrino sources at these energies. The comparison with existing bounds is provided in Fig.9(b). In the currently considered parameter space, there are but a few available limits. We can see the induced solar neutrino CEνNS processes of PandaX-4T and XENONnT are surpassed for $m_4 \lesssim 0.4$ MeV, while these limits dominate the high-mass region up to 10 MeV. Moreover, the sterile-neutrino decay and IceCube/DeepCore bounds occupy the much larger mass region up to the sub-GeV scale.

Lastly, we report the 2 dof results at 90% CL for the flavor-independent case in Fig.10(a). The corresponding upper limits for $m_4 \lesssim 0.03$ MeV are $\mu_{\nu_{\ell 4}} \lesssim 2.22 \times 10^{-11}\mu_{\mathrm{B}}$ for PandaX-4T Run0, $\mu_{\nu_{\ell 4}} \lesssim 1.47 \times 10^{-11}\mu_{\mathrm{B}}$ for PandaX-4T Run1, and $\mu_{\nu_{\ell 4}} \lesssim 0.95 \times 10^{-11}\mu_{\mathrm{B}}$ for XENONnT. Similar with the flavor-dependent cases, we observe significant improvements in the limits from Run0 to Run1, while XENONnT provides the tightest constraint overall. A detailed comparison with earlier results of flavor-dependent cases is presented in Fig.10(b). In general, similar behavior from previous results is found. Supplementary limit from stellar cooling [36] process is added, indicating that our obtained limits dominate the sub-MeV mass scale and are about one order of magnitude away from covering this bound. Overall, the recent low-energy electronic recoil data from direct-detection facilities could provide limit enhancements on the transition magnetic moment compared to other facilities. This comparison highlights the progressive tightening of bounds achieved by the latest datasets.

Table 2. Summary of the derived 90% CL limits (2 dof) on the transition magnetic moments, obtained from the PandaX-4T and XENONnT datasets.

TMM	PandaX-4T		XENONnT
	Run0	Run1	
$\mu_{\nu_{\ell 4}}$	$\lesssim 2.22 \times 10^{-11}\mu_{\rm B}$	$\lesssim 1.47 \times 10^{-11}\mu_{\rm B}$	$\lesssim 0.95 \times 10^{-11}\mu_{\rm B}$
$\mu_{\nu_{e4}}$	$\lesssim 2.97 \times 10^{-11}\mu_{\rm B}$	$\lesssim 1.97 \times 10^{-11}\mu_{\rm B}$	$\lesssim 1.22 \times 10^{-11}\mu_{\rm B}$
$\mu_{\nu_{\mu 4}}$	$\lesssim 4.86 \times 10^{-11}\mu_{\rm B}$	$\lesssim 3.30 \times 10^{-11}\mu_{\rm B}$	$\lesssim 2.01 \times 10^{-11}\mu_{\rm B}$
$\mu_{\nu_{\tau 4}}$	$\lesssim 4.30 \times 10^{-11}\mu_{\rm B}$	$\lesssim 2.82 \times 10^{-11}\mu_{\rm B}$	$\lesssim 1.74 \times 10^{-11}\mu_{\rm B}$

We summarize our 2 dof 90% CL limits in Table 2, clearly illustrating the comparative sensitivity of the considered experiments. We would like to mention that these are compatible with the combined analysis results of LZ, PandaX-4T, and XENONnT studied in Ref. [77] regarding the sterile-active neutrino TMM in the EνES process. Beyond the current experimental constraints, future prospects for probing active–sterile TMMs have been actively explored in the literature. In particular, Ref.[36] provides projected sensitivities for the next-generation multi-ton direct detection experiment DARWIN[78], demonstrating its potential to significantly improve upon existing limits. Similarly, in our previous work [80], we performed a sensitivity analysis using the projected specifications of the CDEX-50 experiment [79] for CEνNS processes, highlighting its complementary reach in the low-energy neutrino sector. Additionally, Ref.[28] investigates expected sensitivities at future forward neutrino detectors such as FLArE[81], designed to probe TeV-scale neutrino interactions at the LHC. Their projections for sterile neutrino dipole portals at high neutrino energies further complement the low-energy direct detection constraints. Overall, our results reinforce the complementarity of the latest direct detection data with other experimental approaches in constraining active–sterile neutrino transition magnetic moments. The growing precision and exposure of current-generation direct detection experiments, combined with future facilities, promise continued progress in probing neutrino electromagnetic properties beyond the SM.

5 Conclusions

Motivated by the availability of recent low-energy electron recoil data from direct detection experiments, we have derived stringent constraints on the active–sterile neutrino transition magnetic moments. The improved sensitivity of facilities such as PandaX-4T and XENONnT to low-energy electron recoils has enabled the observation of solar neutrino fluxes with unprecedented precision, thereby providing an ideal platform to probe the sterile neutrino dipole portal. We have explored both flavor-dependent and flavor-independent scenarios of active–sterile transition magnetic moments, incorporating the effects of neutrino oscillations and flavor conversion in the Sun and Earth.

In this work, we have considered the contributions of both *pp* and ^{7}Be solar neutrino flux components in driving the up-scattering process via a transition magnetic moment into a sterile neutrino state. The analysis includes the day–night asymmetry effect arising from the matter-induced oscillation of neutrinos traversing the Earth, ensuring a comprehensive treatment of solar neutrino propagation effects. We have presented limits at both 1 dof and 2 dof of the sterile neutrino dipole portal, providing a robust statistical interpretation of the results. Our derived constraints are competitive with, and in certain cases surpass, existing bounds obtained from accelerator, reactor, atmospheric, and astrophysical neutrino experiments. Notably, we find that recent advancements in DD experiments have begun to probe the parameter space approaching the sensitivity of constraints derived from supernova observations and cosmological considerations.

The sterile neutrino remains one of the most compelling extensions to the SM, particularly as it may provide insight into the origin of neutrino mass. Our study demonstrates the capability of current-generation DD experiments, using solar neutrinos via elastic neutrino–electron scattering, to explore this phenomenological scenario in a complementary and competitive manner. Looking ahead, future improvements in detector exposure, background suppression, and lower recoil energy thresholds are anticipated to further enhance the sensitivity to neutrino electromagnetic properties. Such developments will enable the next generation of experiments to probe transition magnetic moments at levels previously accessible only via other astrophysical or cosmological observations, offering valuable new tests of BSM physics.

Acknowledgments

This work was supported by the Scientific and Technological Research Council of Türkiye (TUBITAK) under the project no: 124F416.

References

[1] Y. Fukuda *et al.* (Super-Kamiokande Collaboration), Phys. Rev. Lett. **81**, 1562-1567 (1998).

[2] Q. R. Ahmad *et al.* (SNO Collaboration), Phys. Rev. Lett. **87**, 071301 (2001).

[3] Q. R. Ahmad *et al.* (SNO Collaboration), Phys. Rev. Lett. **89**, 011301 (2002).

[4] B. Pontecorvo, Zh. Eksp. Teor. Fiz. **53**, 1717-1725 (1967).

[5] A. Kusenko, Phys. Rept. **481**, 1-28 (2009).

[6] B. Dasgupta and J. Kopp, Phys. Rept. **928**, 1-63 (2021).

[7] A. A. Aguilar-Arevalo *et al.* (MiniBooNE Collaboration), Phys. Rev. Lett. **105**, 181801 (2010).

[8] C. A. Argüelles , I. Esteban, M. Hostert, K. J. Kelly, J. Kopp, P. A. N. Machado, I. Martinez-Soler and Y. F. Perez-Gonzalez, Phys. Rev. Lett. **128**, 241802 (2022).

[9] C. Athanassopoulos *et al.* (LSND Collaboration), Phys. Rev. Lett. **81**, 1774-1777 (1998).

[10] G. C. McLaughlin, J. M. Fetter, A. B. Balantekin and G. M. Fuller, Phys. Rev. C **59**, 2873-2887 (1999).

[11] Z. Xiong, M. R. Wu and Y. Z. Qian, The Astrophysical Journal **880**, 2 (2019).

[12] S. Dodelson and L. M. Widrow, Phys. Rev. Lett. **72**, 17-20 (1994).

[13] A. B. Balantekin and N. Vassh, Phys. Rev. D **89**, 073013 (2014).

[14] A. N. Khan, JHEP **01**, 052 (2023).

[15] A. Mirizzi, N. Saviano, G. Miele and P. D. Serpico, Phys. Rev. D **86**, 053009 (2012).

[16] G. Domokos and S. Kovesi-Domokos, Phys. Rev. D **55**, 2526-2529 (1997).

[17] S. N. Gninenko and N. V. Krasnikov, Phys. Lett. B **450**, 165 (1999).

[18] D. McKeen, and M. Pospelov, Phys. Rev. D **82**, 113018 (2010).

[19] H. Primakoff, Phys. Rev. **81**, 899 (1951).

[20] G. Magill, R. Plestid, M. Pospelov and Y. D. Tsai, Phys. Rev. D **98**, 115015 (2018).

[21] C. Blanco, D. Hooper, and P. Machado, Phys. Rev. D **101**, 075051 (2020).

[22] T. Schwetz, A. Zhoua and Jing-Yu Zhua, J. High Energ. Phys **2021**, 200 (2021).

[23] S. N. Gninenko, Phys. Rev. D **83**, 015015 (2011).

[24] V. De Romeri, O. G. Miranda, D. K. Papoulias, G. Sanchez Garcia, M. Tórtola and J. W. F. Valle, J. High Energ. Phys. **2023**, 035 (2023).

[25] V. De Romeri, D. K. Papoulias and G. Sanchez Garcia, Phys. Rev. D **111**, 7 (2025).

[26] D. Aristizabal Sierra, V. De Romeri and D. K. Papoulias, JHEP **09**, 076 (2022).

[27] P. D. Bolton, F. F. Deppisch, K. Fridell, J. Harz, C. Hati, and S. Kulkarni, Phys. Rev. D **106**, 035036 (2022).

[28] A. Ismail, S. Jana and R. Mammen Abraham, Phys. Rev. D **105**, 055008 (2022).

[29] S. Antusch, E. Cazzato and O. Fischer, Int. J. Mod. Phys. A **32**, 1750078 (2017).

[30] P. Coloma, P. A. N. Machado, I. Martinez-Soler and I. M. Shoemaker, Phys. Rev. Lett. **119**, 201804 (2017).

[31] R. Plestid, Phys. Rev. D **104**, 075027 (2021).

[32] R. A. Gustafson, R. Plestid and I. M. Shoemaker, Phys. Rev. D **106**, 095037 (2022).

[33] M. Atkinson, P. Coloma, I. Martinez-Soler, N. Rocco, and I. M. Shoemaker, J. High Energ. Phys. **2022**, 174 (2022).

[34] O. G. Miranda, D. K. Papoulias, O. Sanders, M. Tortola and J. W. F. Valle, J. High Energ. Phys **2021**, 191 (2021).

[35] Y.-F. Li, and S. Y. Xia, Phys. Rev. D **106**, 095022 (2022).

[36] V. Brdar, A. Greljo, J. Kopp and T. Opferkuch, JCAP **01**, 039 (2021).

[37] G. y. Huang, S. Jana, M. Lindner and W. Rodejohann, Phys. Lett. B **840**, 137842 (2023).

[38] A. B. Balantekin, G. M. Fuller, A. Ray and A. M. Suliga, Phys. Rev. D **108**, 123011 (2023).

[39] X. Zeng *et al.* (PandaX Collaboration), Phys. Rev. Lett. **134**, 041001 (2025).

[40] E. Aprile *et al.* (XENON Collaboration), Phys. Rev. Lett. **129**, 161805 (2022).

[41] M. Demirci and M. F. Mustamin, Phys. Rev. D **111**, 055032 (2025).

[42] M. Demirci, H. I. Sezer, M. F. Mustamin, A. B. Balantekin, accepted to Phy. Rev D, arXiv:2510.12449 [hep-ph].

[43] F. Bergsma *et al.* (CHARM Collaboration), Phys. Lett. B **128**, 361 (1983).

[44] J. Altegoer *et al.* (NOMAD Collaboration), Nucl. Instrum. Meth. A **404**, 96-128 (1998).

[45] C. Arpesella *et al.* (BOREXINO Collaboration), Phys. Lett. B **658**, 101-108 (2008).

[46] M. Deniz *et al.* (TEXONO Collaboration), Phys. Rev. D **81**, 072001 (2010).

[47] M. G. Aartsen *et al.* (IceCube Collaboration), Phys. Rev. D **93**, 022001 (2016).

[48] J. Colaresi, J. I. Collar, T. W. Hossbach, C. M. Lewis and K. M. Yocum, Phys. Rev. Lett. **129**, 211802 (2022).

[49] N. Ackermann *et al.* (CONUS Collaboration), Nature **643**, 1229-1233 (2025).

[50] M. Agostini *et al.* (BOREXINO Collaboration), Nature **562**, 505-510 (2018).

[51] K. Abe *et al.* (Super-Kamiokande Collaboration), Phys. Rev. D **97**, 072001 (2018).

[52] Z. Bo *et al.* (PandaX Collaboration),, Phys. Rev. Lett. **133**, 191001 (2024).

[53] E. Aprile *et al.* (XENON Collaboration),, Phys. Rev. Lett. **133**, 191002 (2024).

[54] J. A. Formaggio and G. P. Zeller, Rev. Mod. Phys. **84**, 1307-1341 (2012).

[55] K. S. Hirata *et al.* (Kamiokande-II Collaboration), Phys. Rev. Lett. **63**, 16 (1989).

[56] S. Fukuda *et al.* (Super-Kamiokande Collaboration), Phys. Rev. Lett. **86**, 5651-5655 (2001).

[57] S. N. Ahmed *et al.* (SNO Collaboration), Phys. Rev. Lett. **92**, 181301 (2004).

[58] B. Aharmim *et al.* (SNO Collaboration), Phys. Rev. Lett. **101**, 111301 (2008).

[59] G. Bellini *et al.* (Borexino Collaboration), Phys. Rev. D **82**, 033006 (2010).

[60] S. Navas *et al.* (Particle Data Group), Phys. Rev. D **110**, 030001 (2024).

[61] J. Erler and S. Su, Prog. Part. Nucl. Phys. 71, 119–149 (2013)

[62] O. Tomalak and R. J. Hill, Phys. Rev. D **101**, 033006 (2020).

[63] M. Atzori Corona, W. M. Bonivento, M. Cadeddu, N. Cargioli and F. Dordei, Phys. Rev. D **107**, 053001 (2023).

[64] P. Vogel and J. Engel, Phys. Rev. D **39**, 3378 (1989).

[65] J. W. Chen, H. C. Chi, C. P. Liu and C. P. Wu, Phys. Lett. B **774**, 656-661 (2017).

[66] K. A. Kouzakov and A. I. Studenikin, Phys. Rev. D **95**, 055013 (2017) [erratum: Phys. Rev. D **96**, 099904 (2017)].

[67] C. C. Hsieh, L. Singh, C. P. Wu, J. W. Chen, H. C. Chi, C. P. Liu, M. K. Pandey and H. T. Wong, Phys. Rev. D **100**, 073001 (2019).

[68] A. Thompson *et al.*, X-ray data booklet (2009).

[69] M. Maltoni and A. Y. Smirnov, Eur. Phys. J. A **52**, 87 (2016).

[70] I. Esteban, M. C. Gonzalez-Garcia, M. Maltoni, T. Schwetz, and A. Zhou, J. High Energ. Phys **2020**, 178 (2020).

[71] D. Zhang *et al.* (PandaX Collaboration), Phys. Rev. Lett. **129**, 161804 (2022).

[72] E. Aprile *et al.* (XENON Collaboration), Phys. Rev. D **102**, 072004 (2020).

[73] S. Baker and R. D. Cousins, Nucl. Instrum. Meth. **221**, 437-442 (1984).

[74] G. L. Fogli, E. Lisi, A. Marrone, D. Montanino and A. Palazzo, Phys. Rev. D **66**, 053010 (2002).

[75] N. Vinyoles, A. M. Serenelli, F. L. Villante, S. Basu, J. Bergström, M. C. Gonzalez-Garcia, M. Maltoni, C. Peña-Garay and N. Song, Astrophys. J. **835**, 202 (2017).

[76] J. N. Bahcall, Neutrino Astrophysics, Cambridge University Press (1989), ISBN: 9780521379755.

[77] V. De Romeri, D. K. Papoulias, G. Sanchez Garcia, C. A. Ternes and M. Tórtola, JCAP **05**, 080 (2025).

[78] J. Aalbers *et al.* (DARWIN Collaboration), JCAP **11**, 017 (2016).

[79] X. P. Geng *et al.* (CDEX Collaboration), JCAP **07**, 009 (2024).

[80] M. Demirci and M. F. Mustamin, Eur. Phys. J. C **85**, 1 (2025).

[81] B. Batell, J. L. Feng and S. Trojanowski, Phys. Rev. D **103**, 075023 (2021).